Nature Communications Main Manuscript for

Organics Guide Non-Classical Crystallization Of Bacterial Calcite Which Parallels Eukaryotic Biomineralization

Franco Grosso Giordano[1,2,3 *], Martín Purino[4], Nico Boon[1], Nele De Belie[2] and Carlos Rodriguez-Navarro[3*]

[1] Ghent University, Center for Microbial Ecology and Technology (CMET), Frieda Saeysstraat 1, 9052, Ghent, Belgium.

[2] Ghent University, Magnel-Vandepitte Laboratory, Dept. of Structural Engineering and Building Materials, Technologiepark Zwijnaarde 60, B-9052, Ghent, Belgium.

[3] University of Granada, Department of Mineralogy and Petrology, 18002, Granada, Spain.

[4] Ghent University, Department of Organic and Macromolecular Chemistry, Krijgslaan 281 S4, B-9000 Ghent, Belgium.

*Corresponding authors: Franco.GrossoGiordano@UGent.be; CarlosRN@Ugr.es.

Keywords: Bacteria, biomineralization, organics occlusion, amorphous calcium carbonate, calcite.

This PDF file includes:

Title page (title, author list, classification, keywords)

Abstract

Main Text

Figures 1 to 6

References

Abstract

Microbially-induced calcium carbonate precipitation is a widespread natural phenomenon with numerous applications. Recent advances have shown that bacterial calcium carbonates (BCC) form non-classically via amorphous calcium carbonate (ACC) precursors in the presence of organics, but the role of organics in the formation and nanostructural features of BCCs is not fully understood. Here we show that different bacterial strains produce BCCs with diverse textural and structural features at the macroscale but similar at the micro and nanoscale. We show that bacterial organics guide precipitation of calcite, stabilizing ACC to produce nanogranular crystals and these organics are then trapped within the crystal, rather than being released as previously suggested. These organics are N-rich and create regions of low Z-contrast aligned perpendicular to the *c*-axis of the crystal, yielding a "Swiss cheese-like" mesostructure. Moreover, it is these occluded organics that lead to the distinctive biosignatures observed in BCC. Finally, we also observe crystalline 2D-structures made up of self-assembled bacterial proteins templating the oriented crystallization of calcite. The formation mechanism and the resulting distinctive nanostructural biosignatures of BCC are strikingly similar to those of carbonate biominerals formed by eukaryotic organisms in controlled biomineralization, suggesting a common origin for this crucial biomineralization process.

Introduction

Biomineralization is a widespread, cross-kingdom phenomenon whereby organisms induce or control the formation of a variety of minerals in or around them [1]. A widely occurring biomineralization process is the precipitation of calcium carbonate. It forms

49 the basis of many current biominerals structures – including shells of molluscs, the
50 cell wall of coralline algae, and the cystolith of plants [1–3] – and ancient – it is the
51 main mineral fraction in microbialites, some of the oldest fossils in the world [4]. The
52 bioprecipitation of calcium carbonate is also a common occurrence in the present day
53 microbial world [5–7], usually denominated as microbially-induced carbonate
54 precipitation (MICP). While calcium carbonate biominerals in eukaryotes is
55 considered to be tightly controlled by genetic and biochemical factors, MICP,
56 generally an extracellular phenomenon, has long been considered uncontrolled with
57 no specific purpose or functionality [8]. However, recent evidence is questioning this
58 notion [9]. For example, calcium carbonates have been reported to lead to an
59 evolutionary benefit by increasing the pathogenic capacity of strains [10], facilitating
60 biofilm formation [11], and providing survival strategies in extreme conditions [12].
61 Formation of intracellular calcium carbonate minerals, a tenant of eukaryote
62 biomineralization, has also been reported in prokaryotes [13].
63
64 Certain aspects of the biochemical understanding of MICP are well agreed upon. For
65 instance, the metabolic pathways of bacterial calcium carbonate (BCC) production
66 are in general well-known and include sulphate reduction [14], photosynthesis [2],
67 denitrification [15] ureolysis and ammonification [16] and metabolism of organic acids
68 [17,18]. Moreover, researchers recognize that there is a role of extracellular polymeric
69 substances (EPS) - which include polysaccharides, proteins and nucleic acids - in the
70 formation of precipitates, acting as a Ca^{2+} adsorption template [19]. Besides their role
71 in concentrating Ca^{2+}, there is growing evidence showing that the organic-mediated
72 formation of amorphous calcium carbonate (ACC) by prokaryotes prior to
73 crystallization of anhydrous $CaCO_3$ appears to be a general phenomena [20–23].
74 Recently, Enyedi et al. [24], showed that bacterial EPS led to long-term stabilization of

ACC, and suggested that the stabilized ACC eventually led to the formation of calcite through non-classical crystallization. However, the MICP crystallization mechanisms are still poorly understood, specifically when the role of organics is involved, while structural aspects of these biocrystals have not been fully characterised.

In contrast, a large body of knowledge has been generated over the last few decades on the formation mechanisms and structure-properties of biomineralized calcium carbonate composites from eukaryotes, mostly of invertebrates such as molluscs (extensively reviewed in *16*), photosynthetic organisms like phytoplankton [26], and biomimetic counterparts [27]. These studies have led to the current model of calcium carbonate biomineralization [28], where most calcium carbonate biominerals form through (nano)particle attachment of ACC precursors, leading to hierarchical structures of different calcium carbonate polymorphs with multiple types of intracrystalline structural modifications including lattice distortions and elemental differences. In turn, these variations in the organic-inorganic hybrid structure leads to different physico-mechanical traits such as the fact that $CaCO_3$ biominerals are often stronger and tougher than geocalcite [25], while they have enhanced abilities to deflect cracking, different dissolution rates and are selectively precipitated as specific polymorphs [25].

It is still important to know that even in the profusely studied eukaryotic calcium carbonates, few studies "have identified the salient nano- and microscale mechanisms" attributed to the material properties of these bio-composites [29]. As such, it is of no surprise that there is a clear knowledge gap in MICP, despite MICP's widespread occurrence, geological significance and bio-engineering applicability [7]. In this work, crystallographic, compositional, textural and (nano)structural differences

101 of BCCs from two bacterial species and inorganic calcite are studied in-depth and at
102 high resolution. The aim is to shed light on the formation mechanism of MICP and
103 study the elemental, compositional and structural characteristics of BCCs at multiple
104 scales. Differences between BCCs and inorganic calcite were starker than between
105 BCCs of the two species and were attributed to the presence of organic
106 biosignatures. Furthermore, BCCs formed through non-classical ACC-to-calcite
107 precipitation and produced crystals with a Swiss-cheese like structure with regions of
108 occluded intracrystalline organic matter. In addition, a bacterially-derived self-
109 assembled 2D structure was identified supporting the role of organic molecules in
110 BCC formation. Overall, these features were starkly similar to those of eukaryotic
111 calcite biominerals. This raises the question whether this precipitation mechanism is
112 common to all $CaCO_3$ biominerals, regardless of their origin (microbial or from other
113 organisms). These findings have implications from an evolutionary standpoint and for
114 technical applications.
115
116 **Results**
117
118 **BCCs have distinctive biosignatures associated with organics and ACC**
119 The calcium carbonate precipitating capacity of two bacterial species was studied to
120 elucidate differences in the mechanistic process of biomineralization. *Lynsinobacillus*
121 *fusiformis* (LMG 9816) strain was used as it has been commonly used in other
122 studies of MICP [30,31]. To test whether nanoscale characteristics between BCCs were
123 similar, a recently isolated strain producing morphologically distinct BCC, *Shouchella*
124 *clausii* (previously known as *Alkalohalobacillus clausii*) LMG 33400, was used. No
125 previous *Shouchella* (or *Alkalohalobacillus)* strain has been reported to precipitate
126 calcium carbonate.

127

128 Optical microscopy imaging (Figure 1a,e) disclosed morphological differences
129 between mineral precipitates produced by *L. fusiformis* and *S. clausii*. *L. fusiformis*
130 mainly produced irregular precipitates with spherical incrustations, while *S. clausii*
131 induced the formation of spherical or oval-shape precipitates. A detailed observation
132 of the latter shows that they display elongated disphenoidal forms, or spindle- and/or
133 dumbbell-shaped structures, as also observed in other bacterial species [32].Both
134 bacteria produced precipitates associated with the bacterial colonies as well as in the
135 surrounding media. Field emission scanning electron microscopy (FESEM) analysis
136 showed the presence of carbonate precipitates closely-associated with organic matter
137 (Figure 1b, f). At the microscale all precipitates had an overall rhombohedral
138 morphology, consistent with the presence of calcite and were better developed in the
139 case of *S. clausii* samples (Figure 1d vs g and h). All of them showed a nanogranular
140 texture, implying formation through particle attachment (PA). In PA, ACC particles
141 100 – 400 nm in size [28] in the presence of organics [33] or crystalline $CaCO_3$
142 nanoparticles [34], attach forming a single crystallographic unit and this is typically
143 observed in carbonate biominerals produced by a range of organisms (e.g., molluscs,
144 barnacles, echinoderms, cnidaria) [27,35–37], including other bacteria [24]. The precipitates
145 were bleached to remove any organics on the precipitate surface and study possible
146 crystallographic and compositional changes. After bleaching, organic matter was not
147 observable anymore on the precipitates (Figure 1c, d and h), calcified bacterial casts
148 could be spotted (Figure 1c), and the crystallographic faces were more obvious
149 (Figure 1h**)**. Note that we performed controls on the sample preparation including
150 the bleaching test with increasing reaction time from 10 up to 480 min, observing
151 (using FTIR) that full removal of surface organics was already achieved after 10 min

(see Supplementary Information and Supplementary Figure 1 and Supplementary Figure 2).

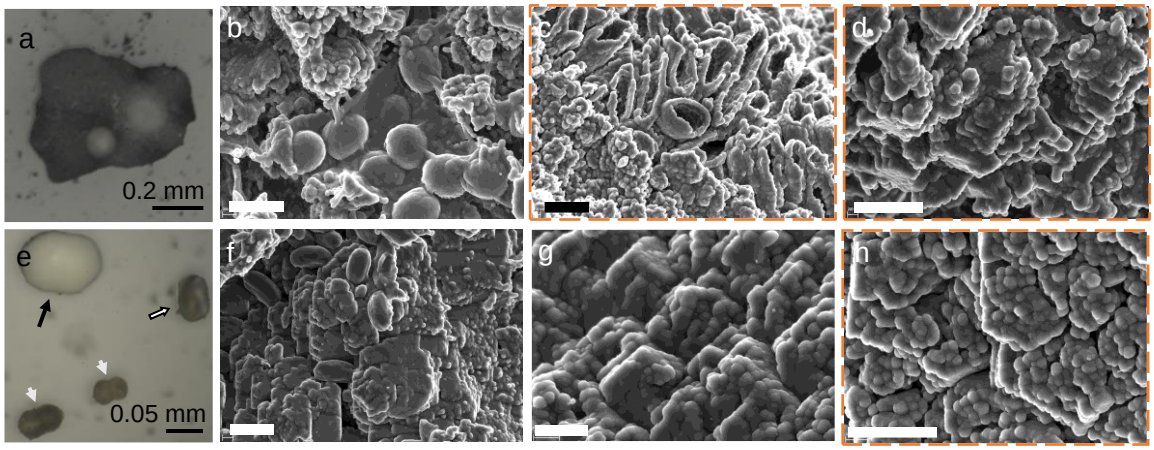

Figure 1. Optical and scanning electron microscopy photomicrographs of bacterial calcium carbonate. Calcium carbonate structures precipitated by *L. fusiformis* (a - d) and *S. clausii* (e - h). Orange outlined images are samples treated with bleach (c, d, h). Different morphologies of calcium carbonate precipitates were produced by both bacteria. (**a**) *L. fusiformis* produced irregular precipitates. (**b**) Bacteria and biofilm associated with precipitated calcium carbonate. (**c**) Bleached *L. fusiformis* precipitates showing the calcified bacterial casts. (**d**) Bleached *L. fusiformis* precipitates (showing rhombohedral vicinal faces) made up of ordered nanoparticles. (**e**) *S. clausii* produced ovoidal (black arrow), disphenoidal (white arrow with black outline) and dumbbell (white arrows) shaped crystals. (**f**) *S. clausii* cells associated with precipitated calcium carbonate (calcite rhombohedra). (**g**) Detail of the mesostructured $CaCO_3$ crystals. (**h**) Bleached calcium carbonate crystals showing the orderly arrangement of calcium carbonate nanoparticles. In all cases the shapeless crystal subunits varying between 100 – 200 nm in size are distinguishable within calcite mesocrystals. All SEM micrograph scale bars are 1.2 μm.

171 XRD confirmed the precipitation of calcite rather than any other calcium carbonate
172 polymorphs. The humps at 10 and 20 - 30 °2θ in the XRD patterns of both *S. clausii*
173 and *L. fusiformis* carbonates pointed to the presence of two distinct amorphous
174 phases (Figure 2a). Note that no humps were present in the XRD pattern of
175 synthesized calcite. Changes in the relative intensity of Bragg peaks were observed
176 for BCCs, as compared with synthetic calcite. Notably, the intensity of the 110 Bragg
177 reflection increased drastically (as compared to the main 104 Bragg reflection). The
178 (110) plane is associated with crystals elongated along the *c*-axis [38] and consistent
179 with the crystal observed in Figure 1. Overdevelopment of {11.0} faces, or more
180 exactly, pseudo-faces composed of (01.2) and (11.0) forms [39], is common in -
181 although not exclusive to - other calcite biominerals and abiotic calcite formed via
182 ACC-to-calcite crystallization in the presence of organics (see Supplementary
183 Information). After bleaching, both humps at 10 °2θ and 20-30 °2θ disappeared.
184 The bleaching of precipitates also led to changes in the intensity of Braggs peaks of
185 both bacterial crystals, most starkly non-(104) planes, with 110 and 113 Bragg
186 reflections being the strongest (Supplementary Table 1) We observed better
187 development of crystal faces after bleaching (Figure 1c, d and h) which would explain
188 the XRD changes.
189

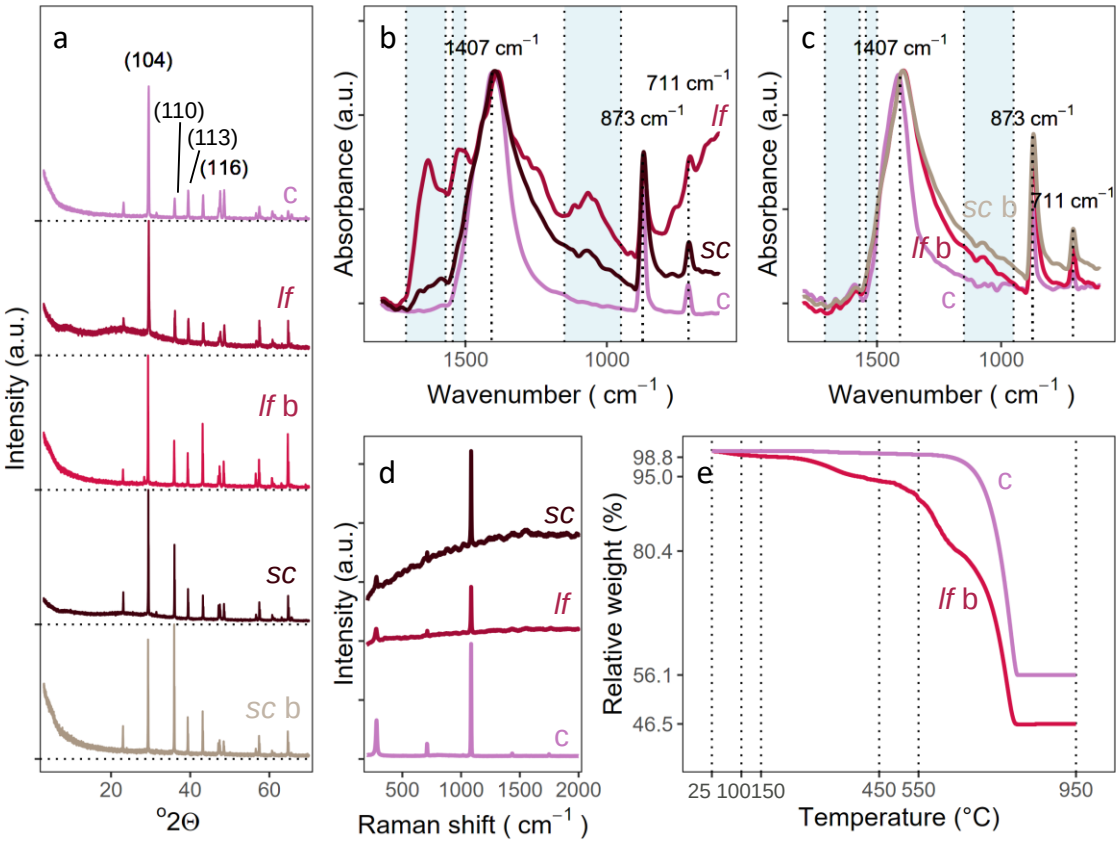

Figure 2. Analysis of synthetic (c, purple) and bacterial crystals (*L. fusiformis* (*lf*, red) and *S. clausii* (*sc,* brown)). Both bacterial calcites were bleached to remove organic matter from the surface (*L. fusiformis* (*lf* b, light red) and *S. clausii* (*sc* b, light brown)) **(a)** XRD patterns of the studied calcium carbonates. Bragg peaks correspond to calcite in all cases and the main *hkl* reflections are indicated. **(b)** FTIR spectra of synthetic, *L. fusifomis* and *S. clausii* calcites. Blue shaded bands indicate organic and/or ACC wavenumber regions. **(c)** FTIR spectra of the calcites after bleaching. **(d)** Raman spectra of the studied unbleached calcites. **(e)** TGA of *L. fusifomis* bleached calcite (light red) vs synthetic calcite (purple).

202 FTIR spectroscopy showed distinctive spectral features among the different
203 precipitates. All precipitates displayed the characteristic v_2, v_3 and v_4 bands of calcite
204 at 873, 1407 and 711 cm^{-1}, respectively, however with some differences. Bacterial
205 calcites showed a slightly red-shifted v_2 band at 869 cm^{-1} (with a broad tail spanning
206 to lower wavenumbers) and a v_3 band at 1402 cm^{-1}. The red-shift of the v_2 band can
207 be caused by ACC which has a characteristic band at 860 cm^{-1} also seen in ACC
208 producing bacterial strains [3,40–43]. There were also variations in the absorbance of the
209 v_2 and v_4 bands. Synthetic calcite had the sharpest and strongest absolute v_4
210 absorbance followed by *S. clausii* and finally by *L. fusiformis* (Figure 2b). Besides the
211 differences in the vibrational modes, certain bands were evident in biogenic
212 precipitates but absent in synthetic calcite: namely between 950 – 1150 cm^{-1}, at
213 1500 – 1550 cm^{-1}, and between 1570 – 1700 cm^{-1}. A last band became apparent at
214 1190 - 1350 cm^{-1}, characteristic of amides [24], when subtracting the synthetic calcite
215 with the BCC spectra (Supplementary Figure S3). Similar spectra have been
216 previously reported on bacterial calcites [24,43,44], attributed to overlapping signatures
217 of organics (general organics at 950 – 1150 cm^{-1} and amides at > 1500 cm^{-1}) and
218 ACC (v_1-mode 1060-1080 cm^{-1}; a v_3 asymmetric vibration at 1470 cm^{-1}; and O-H
219 bending at 1650 cm^{-1} from structural H_2O in ACC) (for details see Supplementary
220 Information). Nevertheless, Mehta and colleagues [43] concluded that it is difficult to
221 infer the presence of ACC from the bands at > 900 cm^{-1} alone.
222
223 Following the bleaching process used to remove organic matter, BCCs produced
224 almost matching FTIR spectra (Figure 2c). No shift was observed in the carbonate v-
225 modes, yet all three modes experienced an increase in absorbance. This is important
226 as changes in calcite v-mode absorbance, most notably the increase in intensity of
227 the 712 cm^{-1} band, is associated with an increase in crystallinity of the carbonates [41].

However, the lack of shift in the v_2 band, and in particular the persistence of the right broad tail, suggests that some ACC was still present, most likely structurally bound to and/or occluded into the BCC calcite structure. Conversely, the increase in v_4 absorption after bleaching suggests that a fraction of ACC, likely the superficially exposed (see TEM results below), was transformed into calcite via dissolution-precipitation in the bleach solution, and/or was removed after rinsing of the bleach. Moreover, the bleaching process leads to removal of bands at higher wavenumbers (bands at 1500 – 1550 cm^{-1} and 1570 – 1700 cm^{-1}), previously linked to organics, pointing to the removal of organics along with ACC. Conversely, the bands at 950 – 1150 cm^{-1} and 1190 – 1350 cm^{-1} also corresponding to organics were conserved after bleaching, with a reduction in absorbance, especially in *L. fusiformis*. Interestingly, the band at 1190 – 1350 cm^{-1} in *L. fusiformis* BCC experienced a shift to higher wavenumber after bleaching. Given that we can associate the wavenumber to the bond strength, a higher wavenumber means that there is a stronger bond of the remaining organics to the crystal structure. It follows that bleaching removed the material more weakly associated with the BCC crystals (e.g. adsorbed organics) and the subsequent rinsing of the bleach, led to dissolution of precursor ACC and recrystallization of calcium carbonate on certain preferential faces of the crystals. This would be responsible for the disappearance of the two humps in the XRD patterns and the changes in Bragg peak intensities. Nevertheless, a fraction of organics (and likely ACC) were not only associated with but structurally bound to the BCC as a signal remains in the FTIR spectra. We suggest that they correspond to intracrystalline occlusions (see TEM and HRXRD below). Duplicates of the BCCs before and after bleaching show consistent FTIR bands (see Supplementary Information and Supplementary Figure 4).

254 Raman spectroscopy analysis showed that all precipitates were identified as calcite
255 with strong fluorescence, but no distinctive spectral feature was identified (Figure
256 2d).
257
258 Thermogravimetric analysis (TGA) was performed on the bleached BCCs of *L.*
259 *fusiformis* and synthetic calcite to further disclose the compositional nature of the
260 biominerals (Figure 2e). The calcite control shows a weight loss of 42.3 % starting
261 from 650 °C, close to the theoretical 44 % due to the decarbonation of calcite. The
262 bleached BCC of *L. fusiformis*, showed a continuous and step-wise mass loss at
263 temperature (*T)* < 100 °C, 150 – 500 °C, 500 – 600 °C and 600 – 950 °C. The initial
264 mass loss is from adsorbed water. The second loss can be from ACC dehydration
265 and/or thermal decomposition of the remaining organic matter. The dehydration of
266 ACC occurs at 100 – 350 °C [42,45] and the decomposition of organic matter starts at
267 250 °C and continues up to 400 or 600 °C for intracrystalline matter [42,46]. Although
268 there is an overlap between both decompositions, the continuous mass loss after 350
269 °C distinguishes the presence of organics. Finally, unlike the control, the weight loss
270 of BCC from 650 - 950 °C (33.9 %) does not match the value corresponding to the
271 theoretical mass loss of $CaCO_3$ following release of CO_2, but rather the weight loss
272 from 550 – 950 does (44.1 %). A lower decomposition temperature in $CaCO_3$ is
273 associated with lower crystallinity [47], which corresponds to the lower crystallinity of
274 BCCs observed with FTIR, and likely related to the possible presence of occluded
275 organics/ACC.
276
277 Overall, it becomes apparent that BCCs produced by the two bacteria studied, when
278 formed, are associated with bacterially-derived organic matter and ACC, with
279 distinctive biosignatures in all tests. FTIR confirmed that bleaching removes a non-

280 calcite fraction, seemingly composed of organics and ACC loosely bound to the
281 crystal surfaces, as seen on the SEM micrographs. But FTIR and TGA results show
282 that there is a non-removable organic/ACC fraction that is more permanently
283 associated with the BCC crystals. Overall this produces biomineralized calcite with
284 non-perfect crystal lattice (i.e. lower crystallinity) due to organics (and likely ACC)
285 occlusion as demonstrated by transmission electron microscopy (TEM) and high
286 resolution synchrotron powder XRD (HRXRD) results (see below).
287

288 **Organics lead to the formation of a distinctive nanostructural Swiss-cheese**
289 **like structure**

290 It could be argued that the bleaching process did not fully eliminate all the organics
291 adsorbed on the BCC precipitates, thereby contributing to their detection by FTIR
292 and TGA analyses. This would thus jeopardise any claim for intracrystalline occlusion
293 of organics, a yet unreported feature of bacterial carbonates. To unambiguously
294 disclose whether intracrystalline organics occlusion took place in BCC calcite, we
295 performed TEM, ss-NRM and HRXRD. .
296

297 Under the TEM we observed that *L. fusiformis* precipitated crystalline (calcite) and
298 amorphous (ACC) phases as confirmed by selected area electron diffraction (SAED)
299 patterns (Figure 3a, Supplementary Figure 5a). Conversely, we could not find
300 individual or aggregated ACC particles in the case of *S. clausii* which only showed
301 single crystal SAED patterns of calcite (Figure 3c). Additionally, SAED patterns with
302 calcite single crystal features were frequently arced, with spots displaying an angular
303 spread of ~4 to 12° on both BCCs (Figure 3c, Supplementary Figure 5a). Angular
304 spreading is a distinctive feature of mesocrystals reflecting a slight misorientation
305 among the different nanocrystals making up a mesocrystal [48] and commonly

associated with the presence of (occluded) organic matter in biominerals [49]. The elemental composition of the unbleached precipitates was confirmed with EDS mapping. Ca, O and C were ubiquitous in all samples. Moreover, it was possible to correlate the presence of organic-related elements such as, N, S and P – the latter two in trace amounts – in the crystals produced by both bacteria (Figure 3b, d, Supplementary Figure 5b, Supplementary Figure 6).

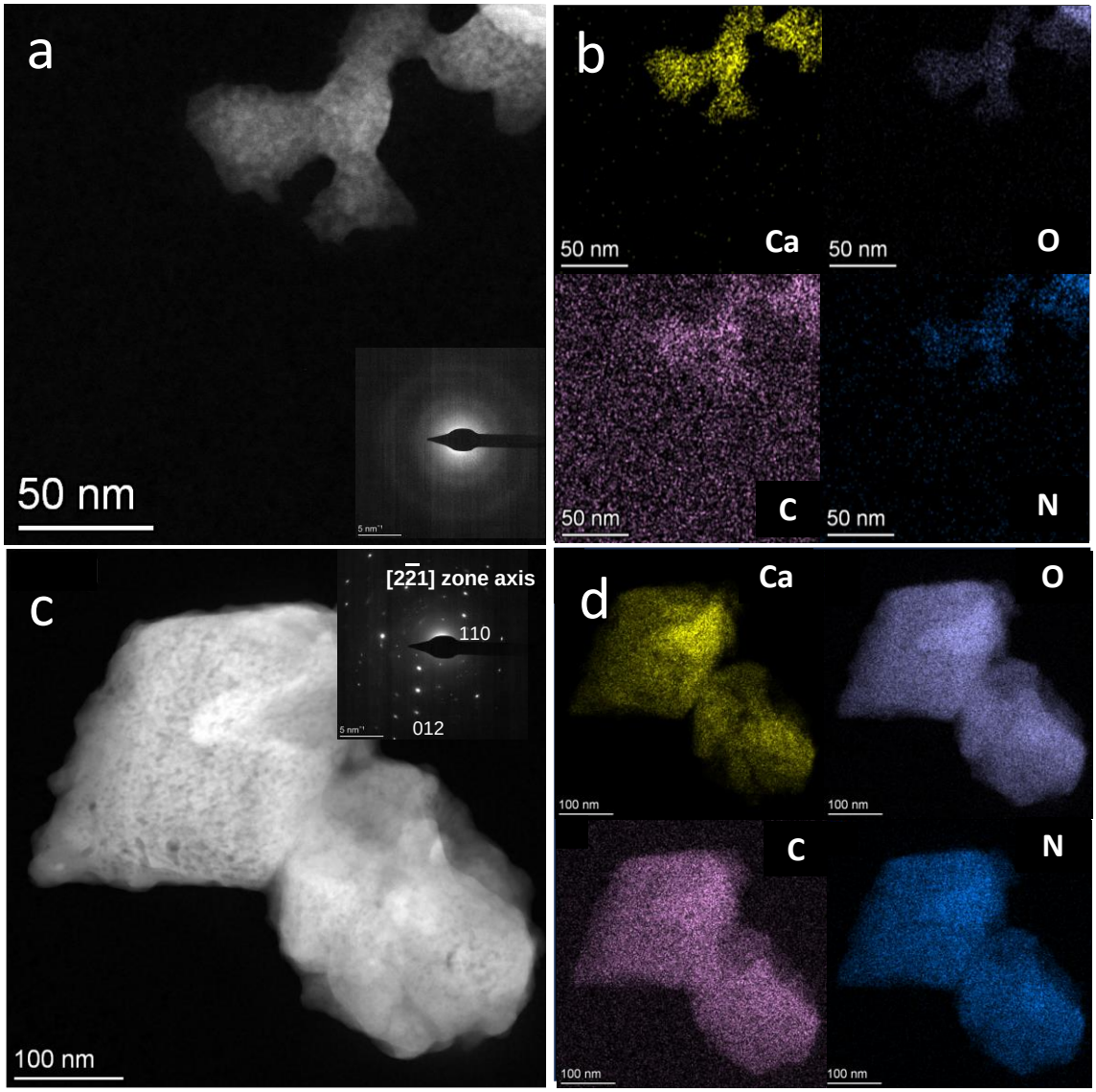

314 **Figure 3. TEM and EDS analysis of bacterial calcium carbonates.** (**a**) HAADF
315 image of ACC precipitated by *L. fusiformis*. Inset: SAED pattern showing the
316 amorphous nature of the particle. (**c**) In clockwise order: EDS elemental maps of
317 precipitates in (a) (calcium, oxygen, nitrogen and carbon, respectively). (**c**) HAADF
318 image of calcite crystals precipitated by *S. clausii*. Note the nanoporous structure of
319 the crystals. Inset: $[2\bar{2}1]$ zone axis SAED pattern of the calcite particle on the left
320 with diffraction spots showing an angular spreading of 6°; (**d**) In clockwise order:
321 EDS elemental maps of precipitates in (D) (calcium, oxygen, nitrogen and carbon,
322 respectively).
323

324

325 EDS line-scans from the edge to the interior of BCC crystals showed that N was not
326 only present within the crystals but also adsorbed on their surface as the intensity
327 did not drop to zero outside the crystal (Figure 4a-d). Point scans showed a lower
328 N:Ca ratio in the centre of the crystals than in the rim (Figure 4e). This implies that
329 the internal areas of the precipitate include a lower relative amount of organics than
330 the rim. To further disclose how the organics were associated with the precipitates,
331 HRTEM analyses were performed, complemented with HAADF-EDS. In the case of *S.*
332 *clausii*, lattice fringe images and corresponding FFT showed that, generally, the
333 outermost layer of the bacterial calcite crystals was amorphous, confirming previous
334 observations [24] (Figure 4f-h, more examples in Supplementary Figure 7). Moreover,
335 here we also observed amorphous areas, interwoven within the crystalline lattice
336 (Figure 4f). This occurred in a region of intermediate contrast and a few nanometers
337 in thickness at the edge of the crystal, which was N-enriched according to EDS
338 analysis (N:Ca ratio of 0.53 Figure 4e). The latter points to occluded organics

including amorphous calcium carbonate, consistent with the relatively high Ca content (Figure 4e).

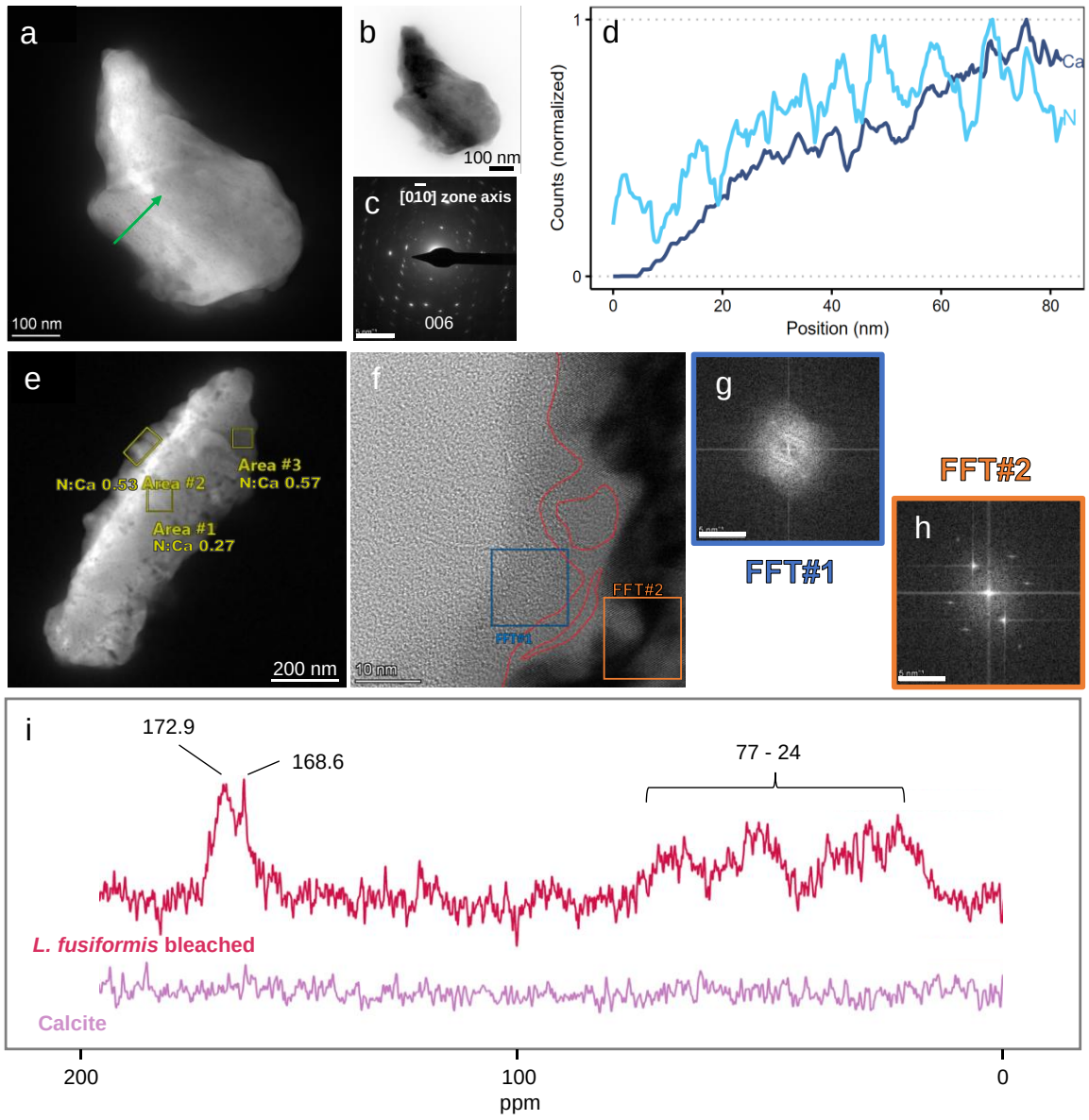

Figure 4. TEM, EDS and ss-NMR analysis of bacterial calcium carbonates. (a) HAADF image of calcite crystal precipitated by *L. fusiformis*. The porous -Swiss-cheese like- structure of the calcite crystal is visible and the location of the EDS line scan is indicated (green arrow). **(b)** Brightfield TEM image of the crystal in (a). **(c)**

347 [$0\bar{1}0$] zone axis SAED pattern of the crystal shown in (a) and (b). Note the marked
348 arcing of diffraction spots (showing an angular spreading of ~9°). **(d)** Line scan in
349 (a) showing that N concentration (light blue line) is uncoupled (after 40 nm) to that
350 of Ca (dark blue line), and the increase in N can be traced to the pores on the calcite
351 crystal (corresponding to the darker areas in (a)). **(e)** *S. clausii* calcium carbonate
352 structure showing different N/Ca ratios in different areas. **(f)** HRTEM image of the
353 edge of the precipitate in (e) (Area #2) with FFT of the blue squared area **(g)**
354 demonstrating it is an amorphous external layer, and the FFT of the orange squared
355 area **(h)** showing it is a crystallized (calcite) internal zone. The red outline
356 demarcates the end of the lattice fringes, showing amorphous areas trapped within
357 the crystalline zone at the rim of the precipitate. **(i)** CP–MAS ^{13}C NMR spectra of
358 bleached *L. fusiformis* calcite (light red) and synthetic calcite (purple). The peak at
359 172 ppm is associated with calcite while the remaining peaks are due to the presence
360 of amides. Referenced to the signal of DSS (δ = 0 ppm).
361
362 Furthermore, an uncoupling of N and Ca was observed on the line-scans in the inner
363 region of the crystals (> 40 nm from the edge), i.e. when Ca increased, N decreased
364 (Figure 4d), albeit with a slight phase-shift. Upon close inspection of HAADF images,
365 it was clear that the crystals did not show a homogenous surface (Figure 4a).
366 Rather, a Swiss cheese-like structure could be observed, with elongated generally
367 parallel low Z-contrast pore-like areas present within the bacterial calcite single
368 crystals (more examples in Supplementary Figure 8). A direct association of these
369 low Z-contrast nanoporous-looking areas with an increase in N content was
370 systematically observed. It could be argued that this porous structure is the result of
371 beam damage. However, this is ruled out here because the HAADF images were
372 collected before EDS analysis and the porous structure was already present.

373 Pioneering work by Towe and Thompson [50], and many other subsequent studies [25]
374 have also shown that beam damage does not produce such features, but organics
375 do. Moreover, this structure was also observed in many other BCCs during brightfield
376 TEM analysis and subsequent SAED analysis showed no CaO diffraction spots/rings
377 which are standard features of beam damage in calcite [51]. Note also that we have not
378 observed such Swiss-cheese structure in any studied synthetic calcite crystal.
379 Although a Swiss-cheese-like structure has never been reported in the case of BCC,
380 similar features have been observed in other calcium carbonate biominerals, such as
381 mollusc shells [25,52], and their biomimetic counterparts [53]. The pore-like areas have
382 been usually identified as intracrystalline organic matter (IOM) and recently with ACC
383 (see Supplementary Information). CP-MAS ^{13}C NMR was used to confirm the nature
384 of those observed here. The CP-MAS ^{13}C NMR spectra of bleached BCC primarily
385 consist of broad peaks, with a notable exception at 168 ppm attributed to calcite
386 (Figure 4i), as confirmed by the MAS ^{13}C of synthetic calcite (Supplementary Figure
387 9). The broad peaks are indicative of amorphous content yet no well-defined peak
388 was observed closely associated downwards of calcite (167 ppm), where ACC is
389 typically present [54]. The remaining option for amorphous content must then be
390 organic in nature. Many broad peaks are present in the 20 - 80 ppm range and a
391 peak at 172 ppm suggests the presence of carbonyl groups. These shifts are linked
392 to amino acids which have peaks at 20-60 ppm (CH), and 170-180 ppm (carbonyl)
393 [55]. Overall, the spectra closely resembles that of eggshells [56] and protein-including
394 calcite biominerals [57].The CP-MAS ^{13}C of the synthetic calcite does not show any
395 bands, as expected (Figure 4i; see also Supplementary Figure 9). This means that
396 the calcite peak present in the *L. fusiformis* BCC is associated with hydrogen atoms,
397 only available from either organics or water [54]. Because the presence of water, such
398 as in monohydrocalcite [54], should broaden and shift to higher ppm values the calcite

399 carbonyl bond, we conclude that the hydrogen is from amine or carboxyl groups
400 from the organics. Lastly, the broadness of the peaks further suggests that the
401 structure is internal [54] in agreement with the fact that the bleaching removed all
402 adsorbed organic matter, but structurally bound organics remained. As such, the
403 observed Swiss cheese-like structure must be present through the whole crystal and
404 not superficially as seemingly observed on TEM.

405 To further disclose whether BCCs included intracrystalline organics, we performed
406 HRXRD analyses at the CRYSTAL beamline of the Soleil synchrotron (France). HRXRD
407 analysis showed that the 104 and 006 Bragg peaks of bleached BCC produced by *L.*
408 *fusiformis* were left-shifted (i.e., to higher *d*-spacings) as compared with geogenic
409 calcite (optical quality Iceland spar) (Figure 5a, b). The shifting was more marked for
410 the 00*l* reflections, implying anisotropic lattice distortion. Rietveld full profile fitting
411 analysis [58] yielded the following refined cell parameters for BCC calcite: a =
412 4.98900(4) Å; c = 17.08345(5) Å; cell volume = 368.24(4) Å^3, demonstrating a
413 clear lattice expansion as compared with reference geogenic calcite (a = 4.98970(2)
414 Å; c = 17.05900(4) Å; cell volume = 367.82(2) Å^3). Maximum lattice strain was
415 observed along the [001] direction ($\Delta c/c$=0.0014). This lattice strain fluctuation is
416 within the range reported for biogenic (e.g., mollusc shell) and biomimetic calcite [59–
417 62]. HRXRD analysis during *in situ* isochronous heating (annealing) from room T up to
418 400 °C at 50 °C intervals (see Materials and Methods), showed little changes in $\Delta a/a$
419 and a significant $\Delta c/c$ reduction at T > 200 °C (Figure 5c). Reanalysis of the BCC
420 after annealing at maximum T and subsequent cooling to room T showed permanent
421 lattice contraction and peak broadening (Figure 5). Pokroy et al. [59,60] observed
422 exactly the same features following similar (isochronous annealing) HRXRD analysis
423 of calcite in mollusc shells, demonstrating intracrystalline occlusion of organics (as
424 solutes) in such biominerals. The preferential expansion along the c-axis was

associated with interaction/replacement of carbonate groups placed along (00.1) planes of calcite by acidic proteins, although interaction with other polar planes such as (01.2) should also be favoured [59,62]. The authors also stated that thermal decomposition of occluded organics at T > 200 °C results in strain relaxation and reduction in $\Delta c/c$, with a parallel increase in peak broadening due to reduction in crystallite size and increase in microstrain fluctuations, as we have observed here. Interestingly, we also observed an increase in $\Delta c/c$ of BCC between 100 °C and 200 °C. The latter, also observed in other calcite biominerals such as sea-urchin spicules, has been associated with the presence of ACC and its thermal-induced transformation into calcite, which leads to expansion [63]. Altogether, our HRXRD results confirm that intracrystalline organics occlusion, with very similar anisotropic lattice distortion as in mollusc shells, also occurs in bacterial calcite. Our HRXRD results also suggest that intracrystalline ACC is present in the BCC structures, as supported by TEM and ss-NMR results.

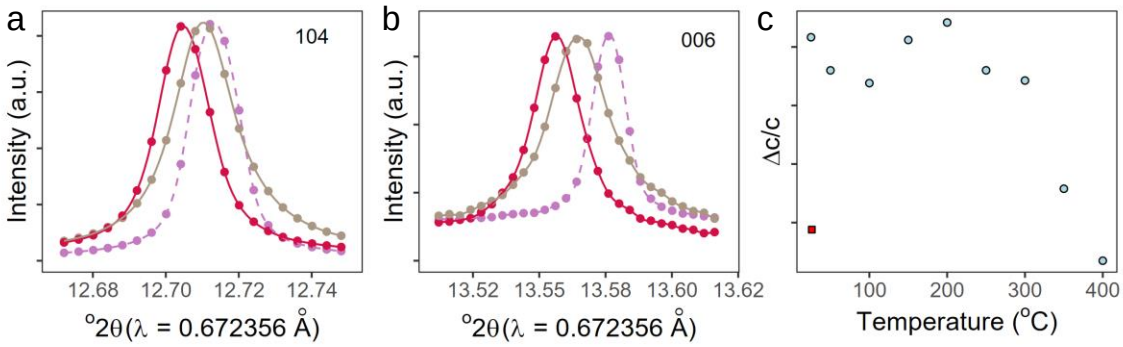

Figure 5. Synchrotron HRXRD analysis of *L. fusiformis* calcite. (a) 104 Bragg peaks and **(b)** 006 Bragg peaks of bacterial calcite before (red) and after annealing at 400 °C and cooling to room T (light brown). The dashed (purple) profiles show the reference geologic calcite; **(c)** T-dependent variation of lattice distortion ($\Delta c/c$) along

445 the *c*-axis as compared with reference geogenic calcite. The red squared symbol
446 marks the residual lattice distortion after annealing at 400 °C and cooling to room *T*.

447 **Role of crystalline 2D organic films in BCC formation**

448 During TEM imaging of *L. fusiformis* biogenic precipitates we unexpectedly observed
449 layered structures containing areas of amorphous and crystalline carbonates (Figure
450 6a). HRTEM imaging showed that these film-like structures were crystalline
451 displaying lattice fringes oriented in different directions and with *d*-spacings of 3.8 –
452 4.3 nm (Figure 6b). Carbonates were closely associated with these 2D crystalline
453 films (Figure 6a, b). SAED analysis of the film-like structures revealed diffraction
454 spots with *d*-spacings 3.7 – 4.5 nm aligned in rows with different orientations
455 corresponding to the multiple orientations of the lattice fringes visualized in the
456 HRTEM image (Figure 6a, yellow and green lines), along with diffraction spots
457 corresponding to (at least two non-oriented) calcite crystals (Figure 6c). The *d*-
458 spacings of the films is at the scale of those measured in protein crystalline
459 structures [64]. The crystalline films were less visible on higher density patches
460 indicating that they were placed at the "bottom" of calcite. However, as shown in
461 Supplementary Figure 10a, we could observe, in other examples, a close relationship
462 between the film and an overlying nanogranular structure of calcite, with a SAED
463 pattern corresponding to a calcite single crystal with a nanogranular structure
464 (Supplementary Figure 10b). These results suggest that the formation of oriented
465 calcite after particle attachment of ACC is templated by the protein film underneath,
466 such as that reported on S-layers [65] or carbonic anhydrase [66] (see Supplementary
467 Information).

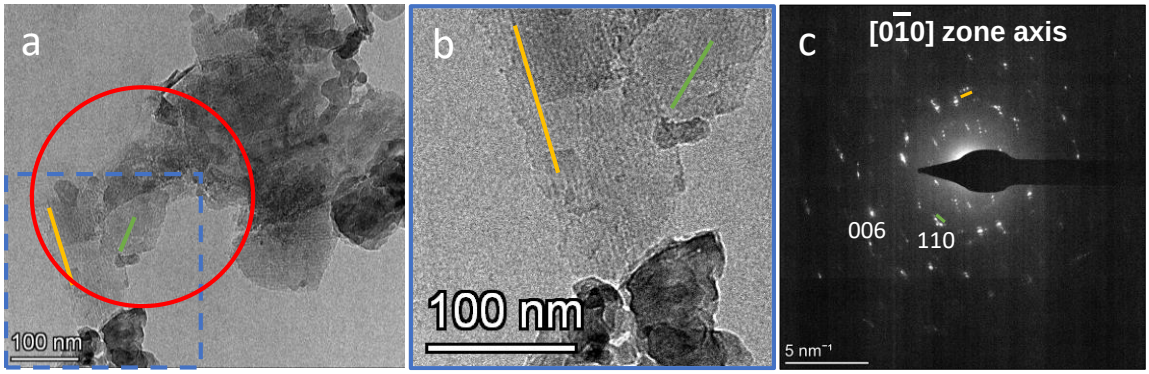

Figure 6. HRTEM analysis of *L. fusiformis* calcite formed on an organic crystalline 2D template. (a) A polycrystal showing different amorphous and crystalline phases, alongside crystalline 2D organic structures showing lattice fringes. **(b)** Zoom-in of the blue squared area in (a) showing lattice fringes in the 2D films. The yellow and green lines show the direction of the lattice fringes. **(c)** SAED pattern of the red circled area in (a) showing different diffraction spots corresponding to calcite ([0$\bar{1}$0] zone axis, calculated using the most intense diffraction spots: note that additional orientations are present) overprinted with diffraction spots of the (organic) films (the green and yellow lines mark the three aligned spots corresponding to the films in (b) with lattice fringes oriented along the green and yellow lines).

Discussion

FESEM showed that the bacteria were closely associated with the BCC crystals and that a nanogranular texture was present suggesting the formation through an ACC precursor. XRD and Raman indicated that all carbonates were calcite, while amorphous and organic signatures were detected with FTIR and TGA, in both bleached and unbleached samples. TEM analysis showed the presence of both crystalline and amorphous calcium carbonate, the latter being more predominant in

489 *L. fusiformis*, in agreement with FTIR spectra. In the individual crystals, amorphous
490 areas were present at the rim of the BCC precipitate, likely the growth front of the
491 crystal, in both bacteria. TEM-EDS mapping unveiled the presence of organic-related
492 elements in the bacterial crystals, including N, (and S and P to a lesser extent)
493 associated with both crystalline and amorphous regions of calcium carbonate
494 precipitates. Importantly, we observed low Z-contrast pore areas that resembled a
495 Swiss cheese-like structure thoroughly reported in calcifying metazoans [36,52], and a
496 strong correlation with N was detected in the low Z-contrast regions. CP-MAS C^{13}
497 NMR pointed at the presence of amino acid in a strikingly similar way as in other
498 protein-including calcite biominerals [57]. TEM-EDS and ss-NMR results helped clarify
499 that the observed FTIR bands correspond to amide bonds (Amide I band (1600 –
500 1700 cm^{-1}); Amide II: 1540 cm^{-1} likely attributed to a C=N bond [67] and C-N-C=O
501 bonds at 1499 cm^{-1} [68]; Amide III band 1250 – 1350 cm^{-1} [68]). Nevertheless, the
502 strong indication of ACC presence throughout the whole study, even after bleaching,
503 suggests that ACC is also occluded, and likely stabilized by the organics [37]. However
504 further analysis is needed to unambiguously prove this. Moreover, HRXRD shows
505 that the amino acids/proteins should be intracrystalline, as there was a marked
506 lattice strain (expansion) along the *c*-axs, and a lattice contraction was observed
507 along the *c*-axis direction after annealing (up to 400 °C). A similar features have
508 been observed using HRXRD in the case of calcite biominerals and their biomimetics
509 (59-61). Note that the nanometer-sized porous areas filled with N-rich organics
510 forming the Swiss-cheese structure are, however, too large to account for the lattice
511 strain fluctuations determined by HRXRD. Apparently, organics are occluded in BCCs
512 at two scales: the atomic scale (as solutes in the calcite crystal lattice) resulting in
513 the observed lattice strain, and the mesoscale (as nanometer-sized clusters) as
514 observed here with TEM as well as in several calcium carbonate biominerals

515 produced by eukaryotes [25]. Note that foreign nanoparticle occlusion results in peak
516 broadening due to microstrain contributions associated with the creation of
517 intracrystalline boundaries acting as a source of inhomogeneous deformation fields
518 but without necessarily contributing to macrostrain, i.e., lattice distortion [60]. These
519 results are consistent with the ss-NMR results as the broad peaks of the CP–MAS ^{13}C
520 NMR spectra point to intracrystalline presence of the amino signatures. Finally, the
521 confirmed role of organics in the crystallization process, explain the preferential
522 growth of BCC calcite along the *c*-axis, with overdeveloped {110} (pseudo)faces,
523 which are typically formed during calcite growth following adsorption of organics on
524 acute steps [69].
525
526 The evidence presented here supports the mechanism of precipitation originally
527 alluded to by Enyedi et al. [24], where ACC is stabilized by EPS, and calcite forms
528 through PA. However, we clarify several missing aspects after ACC stabilization.
529 Firstly, we propose that BCC grows by aggregation of protein-stabilized ACC, rather
530 than the more broadly assigned EPS. This is consistent with the intracrystalline
531 occlusion in BCC calcite crystals of both proteins and ACC. Moreover, we observed
532 that larger crystalline 2D protein structures, not only stabilize, but act as a template
533 for crystal formation. The stabilized ACC then undergoes an amorphous-to-crystalline
534 conversion, at which point the intracrystalline occlusion of a fraction of the organics
535 associated with ACC occurs. This closely resembles the current model of
536 biomineralization of calcite biominerals in eukaryotes [36]. Our proposition is in
537 contrast to what was previously suggested for bacteria, where organics were
538 assumed to be completely ejected [24]. Biomineralization through the eukaryotic model
539 commonly produces a nanogranular structure and results in a Swiss cheese-like
540 structure, as observed here. Even more remarkable, de Frutos and colleagues

541 proposed a model for calcite biomineralization in animals wherein the formation of
542 pellicle-like regions of concentrated organics are formed [36]. These are starkly similar
543 to the orderly fashion in which the pore-like N-rich structures were observed in our
544 bacteria biominerals. Moreover, the transformation of ACC nanoparticles into calcite
545 occurs in crystallographic register with the core calcite, which explains the single
546 crystal features of the SAED patterns. Still, some miss-orientation occurs, resulting
547 in the observed angular spreading and the mesocrystal features described above,
548 which are also observed in calcite biominerals produced by eukaryotes, as it is the
549 case of sea-urchin spicules [70].
550
551 This conserved mechanism of biomineralization between BCC and that reported in
552 biomineralizing protists and metazoan might not be surprising given that many
553 processes proposed for the formation of calcite biominerals have been shown to be
554 thermodynamically favourable (i.e., down-hill energy landscape) [27]. Similar
555 structures seem to form in the case of biomimetic *in vitro* models [53], yet, critically, in
556 these models the carbonate crystals do not display the highly organized organic-
557 inorganic nanostructure observed in biominerals, in general, and in our BCCs, in
558 particular. The organization of the BCCs mesocrystals and the hierarchy in organics
559 occlusion observed in this work contradicts the common idea that calcium carbonate
560 biomineral precipitation by microorganisms - in contrast $CaCO_3$ biominerals produced
561 by eukaryotes - is a spontaneous and uncontrolled phenomenon [8]. Furthermore,
562 other authors are already scrutinizing the idea that calcium carbonate
563 biomineralization in prokaryotes is functionless [71]. Some recent work points to real
564 adaptive benefits for MICP. For example, Botusharova et al. [12] showed that bacterial
565 spores could survive entombment in carbonate precipitates, being autoclaved and
566 then reactivated. More recently, it was shown that the precipitation of calcium

567 carbonate had a central role in the effective formation of biofilm in pathogenic
568 bacteria with genetic inhibition of carbonate biomineralization leading to a reduced
569 pathogenicity and biofilm formation [10]. On the other hand, control over the
570 precipitation process could provide protection to the bacteria from unfavourable
571 conditions by controlling the rate and location on the cell where precipitates form, for
572 example to prevent unwanted entombment [65], or reduce damage from toxic metals
573 by removing these from the surrounding environment through (co)precipitation in
574 carbonates [72]. Although the work remains limited, investing energy in producing
575 organics that will create a controlled process of biomineralization might contribute to
576 the inclusive fitness of the organism. Moreover, stabilized ACC as a precursor prior to
577 transitioning to calcite has been shown in different biomineral composites to lead to
578 improved structural properties [73]. As such, understanding how these mechanisms
579 work and are controlled can open up the door for novel biomaterial applications with
580 purposely designed structure-function.
581
582 The similarities between the formation mechanism (via amorphous phases and PA in
583 the presence of N-rich organics -aminoacids/peptides/proteins-), and the resulting
584 nanostructural and compositional features of the hybrid organic-inorganic BCCs
585 studied here, and $CaCO_3$ biominerals produced by eukaryotes [28] are remarkable. In
586 the case of MICP, the main missing aspect that has been discussed in carbonate
587 biomineralization of eukaryotes is the presence of a privileged space, a biologically
588 controlled compartment where biominerals can form [28]. Here, the observed adsorbed
589 organics on the crystals could act as a rudimentary permeable privileged space
590 where the process of biomineralization (adsorption of Ca^{2+}, high concentration of
591 both DIC and DOC from EPS, formation and stabilization of ACC, and crystallization
592 of calcium carbonate through particle attachment on the growth front) could take

593 place. At a higher organizational scale, this is similar to what has been described in
594 the EPS of microbial mats [74], which further stimulates the possibility of organics and
595 EPS as proto-permeable spaces. Moreover, there is evidence for the intracellular
596 formation of calcium carbonate biominerals (mostly ACC) in some bacteria [13,75] which
597 further points to a conserved mechanism for biomineralization. This prompted us to
598 suggest that there must be a shared "biomineralization pathway" between
599 prokaryotes and eukaryotes [74].
600
601 To open up the debate about whether a conserved process of biomineralization might
602 exist across prokaryotes and eukaryotes, here we propose two possible evolutionary
603 paths based on what is currently known on the evolution and mechanisms of calcium
604 carbonate in other organisms. First, it is the possibility of a eukaryotic-prokaryotic
605 common ancestor already having the molecular toolkit for the formation of calcium
606 carbonate biominerals. Work on biomineralizing animals have shown that the
607 mechanisms of biomineralization emerged independently multiple times through the
608 co-optation of proteins from other processes, with the last common ancestor of all
609 biomineralizing clades today not having the capacity to do so [28]. Nevertheless, some
610 of the currently associated proteins involved in calcium carbonate precipitation - such
611 as carbonic anhydrase - are also present in bacteria [76] alluding at the possibility that
612 the last common ancestor between prokaryotes and eukaryotes might have shared
613 the same ancient co-opted protein toolkit used, for instance, in modern shell
614 formation [77]. The other possibility is that some eukaryotes acquired the protein
615 toolkit from prokaryotes at different stages, either at the beginning of the Cambrian
616 as proposed by [74], or later as supported by the idea of a web of life [78]. This could
617 have occurred through a horizontal gene transfer (HGT) event such as
618 endosymbiosis, gene transfer from host-microbiome interactions or other possible

619 HGT events known to occur between prokaryotes and eukaryotes [79]. For example,
620 work on sea urchins has shown that ACC-precursor forms intracellularly in vacuoles
621 [80] and in coccolithophores the Golgi apparatus is heavily involved in the formation of
622 the calcite coccoliths intracellularly [81]. The endomembrane system in eukaryotes has
623 long been proposed to have been formed as a remnant of an endosymbiotic event
624 [82,83], which would link the formation of extracellular calcium carbonate to the
625 capacity of eukaryotes to develop, at different points in time, the capacity to
626 precipitate calcium carbonate in a controlled environment. Moreover, in case of HGT,
627 incorporation of genetic information commonly has neutral or nearly neutral effects
628 in the recipient [78]. This means that the genes are not expressed or only to a limited
629 extent and provide peripheral functionality. Only after the acquisitions do these
630 genes change and provide a novel beneficial phenotype. Acquiring genes through a
631 HGT event could explain the lack of a biomineralizing common ancestor [84], either
632 because there were multiple HGT events or an original neutral HGT event. Naturally,
633 the malleability of the molecular toolkit would have led to the multiple variations in
634 different marine animals we observe today [85]. The possibility that HGT from bacteria
635 to eukaryotes could be at the root of carbonate biomineralization in higher order
636 organisms is consistent with experimental results showing that bacterial precipitation
637 of calcium carbonates is associated with specific genes [86]. Mutants without such
638 genes were unable to produce BCC.
639
640 Besides the evolutionary standpoint, there is the technical applicability of the results.
641 The observations of intracrystalline organics implies that there might be improved
642 mechanical properties for BCC, as occurs with other calcium carbonate biominerals
643 such as mollusk shells (i.e., increased toughness) [25], which can have implications in
644 the industrial applications of MICP, like self-healing cements or the consolidation of

stone built heritage. Moreover, identification of these biosignatures could pave the way for determining biogenicity of carbonate samples in the geologic record, which is not always straight forward.

Materials and Methods

Synthetic calcite preparation

Calcite was produced synthetically in order to act as an abiotic control. A reaction pathway was chosen as proxy to that expected in the bacterial cultures, whereby calcite precipitated by the dissolution of CO_2 from bacterial respiration. A saturated calcium hydroxide solution was prepared by adding 5 g $Ca(OH)_2$ to 100 ml of distilled water, stirring for 30 min at 50 RPM and letting sit for 2 h. The supernatant (i.e., a saturated solution of Ca^{2+} and OH^- (equation 1) was poured into a clean container. CO_2 was then purged through this solution. This enabled the fast dissolution and hydration of CO_2, creating bicarbonate (equation 2) and carbonate ions (equation 3 or 4). Subsequently, $CaCO_3$ spontaneously precipitated through the reaction of carbonate ions with Ca^{2+} (equation 5) in the absence of any background electrolyte. The precipitates were filtered using a vacuum pump and polycarbonate filters (φ = 0.22 μm). The filter with the precipitates was placed at room temperature (*T*) and dried overnight. The dry solids were stored in plastic vials for further analysis.

$$Ca(OH)_2 \rightarrow Ca^{2+} + 2OH^- \qquad (1)$$

$$OH^- + CO_2 \rightarrow HCO_3^- \qquad (2)$$

$$HCO_3^- + OH^- \rightarrow CO_3^{2-} + H_2O \qquad (4)$$

$$Ca^{2+} + CO_3^{2-} \rightarrow CaCO_3 \qquad (5)$$

671 **Selection and cultivation of bacterial strains**

672 Two bacterial strains were used in this study, *Lynsinobacillus fusiformis* (LMG 9816)
673 and a recently isolated strain, *Shouchella clausii* (registered at the Belgian
674 Coordinated Collection of Microorganisms as LMG 33400). *S. clausii* was isolated
675 from a lime mortar wall in Ghent, Belgium by selecting morphologically distinct
676 colonies from a Horikoshi medium. Its capacity for carbonate precipitation was tested
677 on B4. Finally, the strain was selectively adapted to high pH tolerance by repeated
678 inoculation in TSB adjusted to pH 11 with CAPS buffer. An alkaliphile was desirable
679 as MICP commonly occurs in alkaline environments. The bacteria were grown and
680 kept in TSA at 28 ^{o}C.

681

682 **Culture and precipitation media, and precipitate extraction**

683 Due to the alkaliphilic nature of both bacteria, carbonate precipitation experiments
684 were carried out on pH 8-adjusted B4-medium, a complex medium used to study
685 precipitation of calcium carbonate crystals [5]. Importantly, Ca-acetate was filter
686 sterilized as doing otherwise would lead to precipitation of calcium carbonate either
687 through too high pH or through heating of the Ca-acetate. For the inoculation of B4
688 plates, bacteria were inoculated in TSB and grown for 48 h. Subsequently, 10 µL of a
689 fully grown culture was drop-inoculated onto 9 spots on B4 plates. The cultures were
690 grown for 4 weeks at 28 °C. At this point, precipitates were visible on the plate and
691 were extracted. Briefly, the B4 agar was cut into pieces and placed in a glass
692 container and melted in a microwave oven. 100 mL of warm deionized water were
693 added to the beaker to dilute the melted agar. The dilute agar was centrifuged at
694 5000 rpm for 1 min while still warm. The pellet was then microwaved again, warm
695 water was added, and centrifuged again. This was performed a third time but
696 centrifuged at 7000 rpm. The sample was warmed up once more, and the suspension

697 was filtered using a vacuum pump and polycarbonate filters (φ = 0.22 μm). The
698 filter with the precipitates was placed at room temperature and dried overnight.
699 Once dried, the solids were placed in a plastic vial for further analysis.
700
701 **Bleaching of precipitates**
702 A fraction of the bacterial precipitates was bleached to remove any potential organic
703 matter on their surfaces [36]. Bleaching was done using commercial bleach and
704 deionized water (1:1 dilution) poured in an Eppendorf tube (1.5 mL) filled with 0.1 g
705 solids, followed by incubation for 2 h in a shaking table. The samples were then
706 centrifuged for 1 min at 5000 RPM and the supernatant discarded. Bleached solids
707 were resuspended in MilliQ water, vortexed for 1 min, and centrifuged again.
708 Washing was performed thrice. The precipitates were dried at 50 °C overnight.
709 Raman and FTIR spectroscopy

710 Precipitates were observed under a Horiba XploRA PLUS Raman spectrometer
711 equipped with a CCD detector (OE., 1024 x 256 pixel, TE deep-air cooled at -60° C,
712 UV-NIR range), an integrated confocal microscope and a built-in camera. Microscopic
713 observations were performed simultaneously with micro-Raman spectra acquisition
714 (excitation with a 4 mW power diode laser operated at 532 nm; frequency range
715 400–4000 cm^{-1}; spectral resolution of 2 cm^{-1}). Averaged values of three spectra (60
716 s acquisition time) for each analyzed spot are reported here. Calibration was
717 performed using the 520.5 cm^{-1} band of silicon in a calibration objective. Samples
718 were observed with the integrated microscope of Raman.

719 Fourier Transform Infrared Spectroscopy (FTIR) spectra of the precipitate were
720 recorded on a NICOLET 20SXB FTIR (400–4000 cm^{-1} spectral range; resolution of 2

721 cm^{-1}). Baseline and smoothing corrections to the FTIR spectra was performed using
722 Spectragryph v1.2.16.1.

723 **X-ray diffraction (XRD)**

724 The crystallographic features of the synthetic (control) and bacterial precipitates
725 were analysed with a Xpert Pro X-ray powder diffractometer (Panalytical, The
726 Netherlands) in reflection mode using copper radiation to determine θ−2θ scans
727 (measurement parameters: Cu Kα radiation λ = 1.5405 Å, 45 kV, 40 mA, 3 to 70°
728 exploration range, with 0.00418° step size and 29.8 s integration time per step).
729 Bacterial precipitates were analysed in zero-background Si sample holders. XRD
730 patterns were analysed using the computer program HighScore Plus Version 3.0d.

731 **TG analysis**

732 Thermogravimetric analysis (TGA) was performed using a TGA 2 (Mettler-Toledo,
733 Switzerland) with a large furnace and an autosampler, using 70 µL alumina crucibles.
734 Samples (12 mg) were heated at 20 °C/min from 25 to 950 °C under air atmosphere
735 (80 mL/min).

736 **Synchrotron High-Resolution Powder X-Ray Diffraction (HRXRD)**

737 HRXRD analyses were performed at beamline CRYSTAL of the SOLEIL synchrotron
738 (Paris, France). The wavelength 0.672356 Å (18.44024 keV) was selected with a
739 double-crystal Si (111) monochromator and determined by using Si640d NIST
740 standard (*a* = 5.43123 Å). The CRYSTAL beamline is equipped with a high-
741 throughput position sensitive detector (PSD) MYTHEN, optimal for time-resolved
742 experiments. Borosilicate glass capillaries of 0.3 mm diameter were loaded with
743 powder samples and rotated during data collection to improve diffracting particle
744 statistics. Isochronous annealing (10°C min^{-1}; 30 s stabilization time at target *T*,
745 tolerance ± 5°C) was performed using a Cyberstar hot gas blower with a Eurotherm

746 *T* controller (Eurotherm, Worthing, UK), collecting diffraction data each 50°C during
747 the heating ramps (50° to 400°C). Once the maximum *T* was reached, the samples
748 were cooled to room *T*, and a final measurement was taken. The data acquisition
749 time was ~5 min per pattern, with up to two iterations per measurement to obtain a
750 good signal-to-noise ratio over the 0-55.34 °2θ angular range. To calibrate the
751 equipment and reduce possible shifts during experimental analysis, a LaB6 standard
752 was used. An instrumental resolution factor analysis was performed in each case.
753 Under these data acquisition conditions, the angular resolution was better than
754 0.006° FWHM. As opposed to conventional XRD, such an angular resolution enables
755 to detect lattice strains of 10^{-3} to 10^{-4} associated with intracrystalline organics.

756 The Rietveld refinement method [58] was used to extract lattice parameters of calcite
757 matching the experimental diffraction peaks with those included in Markgraf and
758 Reeder [87] using Topas software. Optical quality (highly pure) geologic calcite (Iceland
759 spar, from Chihuahua, Mexico) was used as standard to compare XRD data from
760 BCC.

761 To investigate the microstructural variations due to organic (macro)molecule
762 incorporation in the calcite structure, the Thompson-Cox-Hastings pseudo-Voigt
763 function was used to fit the profile of the experimental diffraction patterns.
764 Refinement cycles were performed to ensure reproducibility of each analysis,
765 selecting a Goodness of Fit of <9. Note that, as opposed to BCC, in the case of the
766 Iceland spar control no changes in Bragg peak position or broadening (FWHM) were
767 observed after annealing, i.e., after returning to room *T* following heating up to
768 400°C. These results show that the selected geogenic calcite is a proper reference to
769 compare the results of BCC HRXRD analysis.

770 **FESEM and TEM analysis**

771 Field Emission Scanning electron microscopy (FESEM) images were collected using
772 an Auriga (Zeiss, Germany) microscope with field emission gun operated at 5 kV. All
773 samples were carbon coated prior to imaging.

774 Nanoscale features and elemental composition of the precipitates were studied using
775 TEM on a Titan (FEI) with acceleration voltage of 300 kV. The TEM was equipped
776 with a high angle annular dark field (HAADF) detector for Z-contrast imaging and
777 energy dispersive X-ray spectroscopy (EDS) for microanalysis (performed in STEM
778 mode). Right before TEM analysis the solids were dispersed in ethanol, sonicated for
779 2 min and fished with carbon-coated TEM Cu grids. Imaging was performed using a
780 20 μm objective aperture, which is a good compromise for amplitude and phase
781 contrast (high resolution, HRTEM) imaging. Selected area electron diffraction (SAED)
782 patterns were collected from areas ~200 nm in diameter.

783 **Solid-state NMR (ssNMR)**

784 The 1D experiments were recorded on a Bruker Ascend 500.13MHz Avance III
785 spectrometer equipped with a Bruker broadband 4 mm 1H/X dual channel CP-MAS
786 smartprobe probe head, equipped with Z-gradients, a MAS III pneumatic unit and
787 running Topspin 3.6.5. For each measurement, the spinning frequency was set to
788 12000Hz, all measurements were performed at room temperature (25°C) and
789 controlled with a Eurotherm 2000 BVT controller and a BCU-I.

790 All samples were prepared by filling the 4mm Bruker K1910 ZrO2 rotors with an
791 appropriate amount of dry and finely grained sample material (25-30 mg per
792 sample). Using subsequent rounds of filling and packing the rotor led to a tightly
793 filled rotor sample for each material under study. Following the packing of the rotors,
794 each of them was sealed with a Kel-F insert, a Kel-F rotor cap and visually checked
795 for any leftover voids or air pockets.

796 The spectra recorded on the samples included 1D ^{1}H and 1D ^{13}C measurements. For
797 the 1D ^{1}H 'onepulse' experiments, the spectral width used was 200.00 ppm with 4
798 scans of 4K data points each being accumulated, preceded by 2 dummy scans and a
799 relaxation delay of 2 seconds. Finally, the spectrometer excitation frequency was set
800 on resonance with the frequency (5 ppm) of the most intense signal. Processing
801 consisted of one order of zero filling to 16K real data points, followed by Fourier
802 transformation, phase correction and a base-line correction.

803 For ^{13}C measurements a 'hpdec' measurement type was used for non-cross-
804 polarization and 'hX.cp' for measurements with cross-polarization (CP) with ^{1}H. The
805 spectral width used was 300.00 ppm with 2048 scans of 4K data points each being
806 accumulated, preceded by 4 dummy scans and a relaxation delay of 5 seconds.
807 Finally, the spectrometer excitation frequency was set on resonance with the
808 frequency (100 ppm) of the most intense signal. Processing consisted of one order of
809 zero filling to 16K real data points, followed by Fourier transformation, phase
810 correction and a base-line correction.

811 Chemical shifts were indirectly referenced by adapting the magnet 'field' value -by
812 measuring an adamantane reference sample-, and adapting the magnet field until
813 one of the adamantane signals is at the right chemical shift value (37.77 ppm). All
814 spectra were processed using TOPSPIN 4.1.3.

815 **Acknowledgments**

816 We thank the personnel of the Centro de Instrumentación Científica (CIC) of the
817 University of Granada for helping with FESEM and TEM analyses and the Inorganic
818 Chemistry department for access to their FTIR. Additional thanks go to the personnel
819 of the Department of Mineralogy and Petrology of the University of Granada for their
820 help with the instrumentations, including Teodora Ilić, Sarah Bonilla Correa, Aurélie

Pace and Miguel Burgos Ruiz. Special thanks go to Kerstin Elert for her help with the SEM imaging and Prof. Fadwa Jroundi Mesbahi for allowing to grow our bacterial cultures at her facilities. HRXRD experiments were performed at CRYSTAL beamline at SOLEIL Synchrotron with the help of this beamline staff (E. Elkaim). We also thank J. Atienzar, A. Pace, and N. Pujol Solà for their help during HRXRD analyses at SOLEIL synchrotron and Alejandro Rodriguez-Navarro for his help during Rietveld analysis of HRXRD results.

Author Contributions:

FGG contributed Conceptualization, Methodology, Investigation, Visualization, Supervision, Writing (original draft), Writing (review and editing)

MP contributed Conceptualization, Investigation, Visualization, Writing (original draft), Writing (review and editing)

NB contributed Conceptualization, Supervision, Writing (review and editing), Funding acquisition

NDB contributed Conceptualization, Supervision, Writing (review and editing), Funding acquisition

CR-N contributed Conceptualization, Methodology, Investigation, Visualization, Supervision, Writing (original draft), Writing (review and editing), Funding acquisition

Competing Interest Statement: The authors declare no competing interest.

Funding: This work was funded by Spanish Government grant PID2021.125305NB.I00 funded by MCIN/ AEI /10.13039/501100011033 and by ERDF A way of making Europe (to C.R.-N.); Junta de Andalucía and ERDF grant B-

RNM-574-UGR20 and research group RNM-179 (to C.R.-N.); University of Granada, Unidad Científica de Excelencia UCE-PP2016-05 (to C.R.-N.). Funding was also provided by the European Union's Horizon 2020 research and innovation programme under Marie Sklodowska-Curie project SUBLime [Grant Agreement n◦955986]. 500 MHz CP-MAS ssNMR was funded by Hercules foundation AUGE/09/2006 and FWO I006920N.

Data availability: All necessary data to evaluate our conclusions are included within the manuscript and the Supplementary Information.

References

1. Lowestam, H. A. & Weiner, S. *On Biomineralization*. (Oxford University Press, New York, 1989).
2. Raven, J. A. & Giordano, M. Biomineralization by photosynthetic organisms: Evidence of coevolution of the organisms and their environment? *Geobiology* **7**, 140–154 (2009).
3. Addadi, L., Raz, S. & Weiner, S. Taking advantage of disorder: Amorphous calcium carbonate and its roles in biomineralization. *Adv. Mater.* **15**, 959–970 (2003).
4. Schopf, J. W. Solution to Darwin's dilemma: Discovery of the missing Precambrian record of life. *Proc. Natl. Acad. Sci. U. S. A.* **97**, 6947–6953 (2000).
5. Boquet, E., Boronat, A. & Ramos-Cormenzana, A. Production of Calcite (Calcium Carbonate) Crystals by Soil Bacteria is a General Phenomenon. *Am. J. Med. Sci.* **242**, 527 (1973).

870 6. Fujita, Y., Grant Ferris, F., Daniel Lawson, R., Colwell, F. S. & Smith, R. W.
871 Calcium carbonate precipitation by ureolytic subsurface bacteria. *Geomicrobiol.*
872 *J.* **17**, 305–318 (2000).
873 7. Seifan, M. & Berenjian, A. Microbially induced calcium carbonate precipitation:
874 a widespread phenomenon in the biological world. *Appl. Microbiol. Biotechnol.*
875 **103**, 4693–4708 (2019).
876 8. Frankel, R. B. & Bazylinski, D. Biologically Induced Mineralization by Bacteria.
877 *Rev. Mineral. Geochemistry* **54**, 95–114 (2003).
878 9. Cosmidis, J. & Benzerara, K. Why do microbes make minerals? *Comptes*
879 *Rendus - Geosci.* **354**, 1–39 (2022).
880 10. Cohen-Cymberknoh, M. *et al.* Calcium carbonate mineralization is essential for
881 biofilm formation and lung colonization. *iScience* **25**, 104234 (2022).
882 11. Oppenheimer-Shaanan, Y. *et al.* Spatio-temporal assembly of functional
883 mineral scaffolds within microbial biofilms. *npj Biofilms Microbiomes* **2**, 15031
884 (2016).
885 12. Botusharova, S., Gardner, D. & Harbottle, M. Augmenting Microbially Induced
886 Carbonate Precipitation of Soil with the Capability to Self-Heal. *J. Geotech.*
887 *Geoenvironmental Eng.* **146**, 04020010 (2020).
888 13. Benzerara, K. *et al.* Intracellular Ca-carbonate biomineralization is widespread
889 in cyanobacteria. *Proc. Natl. Acad. Sci. U. S. A.* **111**, 10933–10938 (2014).
890 14. Baumgartner, L. K. *et al.* Sulfate reducing bacteria in microbial mats:
891 Changing paradigms, new discoveries. *Sediment. Geol.* **185**, 131–145 (2006).
892 15. Erşan, Y. Ç., De Belie, N. & Boon, N. Microbially induced CaCO3 precipitation
893 through denitrification: An optimization study in minimal nutrient environment.
894 *Biochem. Eng. J.* **101**, 108–118 (2015).
895 16. Stocks-Fischer, S., Galinat, J. K. & Bang, S. S. Microbiological precipitation of

896 CaCO3. *Soil Biol. Biochem.* **31**, 1563–1571 (1999).
897 17. Rivadeneyra, M. A., Delgado, R., Moral, A., Ferrer, M. R. & Ramos-
898 Cormenzana, A. Precipatation of calcium carbonate by Vibrio spp. from an
899 inland saltern. *FEMS Microbiol. Ecol.* **13**, 197–204 (1994).
900 18. Ehrlich, H. L. *Ehrlich's Geomicrobiology*. *Ehrlich's Geomicrobiology* (Taylor &
901 Francis, 2016).
902 19. Tourney, J. & Ngwenya, B. T. The role of bacterial extracellular polymeric
903 substances in geomicrobiology. *Chem. Geol.* **386**, 115–132 (2014).
904 20. Benzerara, K. *et al.* Nanoscale detection of organic signatures in carbonate
905 microbialites. *Proc. Natl. Acad. Sci. U. S. A.* **103**, 9440–9445 (2006).
906 21. Lyu, J. *et al.* Bacterial templated carbonate mineralization: insights from
907 concave-type crystals induced by Curvibacter lanceolatus strain HJ-1. *RSC*
908 *Advances* vol. 14 353–363 at https://doi.org/10.1039/d3ra06803j (2024).
909 22. Lyu, J., Qin, W., Zhang, C. & Li, F. Nanoparticle Accumulation in Microbial
910 Induced Carbonate Precipitation: The Crucial Role of Extracellular Polymeric
911 Substance. *Geomicrobiol. J.* **0**, 837–847 (2020).
912 23. Chen, L. *et al.* Bacteria-mediated synthesis of metal carbonate minerals with
913 unusual morphologies and structures. *Cryst. Growth Des.* **9**, 743–754 (2009).
914 24. Enyedi, N. T. *et al.* Cave bacteria-induced amorphous calcium carbonate
915 formation. *Sci. Rep.* **10**, 1–12 (2020).
916 25. Deng, Z., Jia, Z. & Li, L. Biomineralized Materials as Model Systems for
917 Structural Composites: Intracrystalline Structural Features and Their
918 Strengthening and Toughening Mechanisms. *Adv. Sci.* **9**, 2103524 (2022).
919 26. Brownlee, C., Wheeler, G. L. & Taylor, A. R. Coccolithophore biomineralization:
920 New questions, new answers. *Semin. Cell Dev. Biol.* **46**, 11–16 (2015).
921 27. Rodríguez-Navarro, C., Ruiz-Agudo, E., Harris, J. & Wolf, S. E. Nonclassical

922 crystallization in vivo et in vitro (II): Nanogranular features in biomimetic
923 minerals disclose a general colloid-mediated crystal growth mechanism. *J.*
924 *Struct. Biol.* **196**, 260–287 (2016).
925 28. Gilbert, P. U. P. A. *et al.* Biomineralization: Integrating mechanism and
926 evolutionary history. *Sci. Adv.* **8**, (2022).
927 29. Wegst, U. G. K., Bai, H., Saiz, E., Tomsia, A. P. & Ritchie, R. O. Bioinspired
928 structural materials. *Nat. Mater.* **14**, 23–36 (2015).
929 30. Yan, H. *et al.* The bio-precipitation of calcium and magnesium ions by free and
930 immobilized Lysinibacillus fusiformis DB1-3 in the wastewater. *J. Clean. Prod.*
931 **252**, 119826 (2020).
932 31. Park, S. J., Park, Y. M., Chun, W. Y., Kim, W. J. & Ghim, S. Y. Calcite-Forming
933 Bacteria for Compressive Strength Improvement in Mortar. *J. Microbiol.*
934 *Biotechnol.* **20**, 782–788 (2010).
935 32. Chekroun, K. Ben *et al.* Precipitation and growth morphology of calcium
936 carbonate induced by Myxococcus xanthus: Implications for recognition of
937 bacterial carbonates. *J. Sediment. Res.* **74**, 868–876 (2004).
938 33. Rodriguez-Navarro, C., Burgos Cara, A., Elert, K., Putnis, C. V. & Ruiz-Agudo,
939 E. Direct Nanoscale Imaging Reveals the Growth of Calcite Crystals via
940 Amorphous Nanoparticles. *Cryst. Growth Des.* **16**, 1850–1860 (2016).
941 34. De Yoreo, J. J. *et al.* Crystallization by particle attachment in synthetic,
942 biogenic, and geologic environments. *Science (80-.).* **349**, (2015).
943 35. Wolf, S. E. *et al.* Nonclassical crystallization in vivo et in vitro (I): Process-
944 structure-property relationships of nanogranular biominerals. *J. Struct. Biol.*
945 **196**, 244–259 (2016).
946 36. de Frutos, M., Rodríguez-Navarro, A. B., Li, X. & Checa, A. G. Nanoscale
947 Analysis of the Structure and Composition of Biogenic Calcite Reveals the

948 Biomineral Growth Pattern. *ACS Nano* **17**, 2829–2839 (2023).
949 37. Gong, Y. U. T. *et al.* Phase transitions in biogenic amorphous calcium
950 carbonate. *Proc. Natl. Acad. Sci. U. S. A.* **109**, 6088–6093 (2012).
951 38. DeOliveira, D. B. & Laursen, R. A. Control of calcite crystal morphology by a
952 peptide designed to bind to a specific surface. *J. Am. Chem. Soc.* **119**, 10627–
953 10631 (1997).
954 39. Teng, H. H. & Dove, P. M. Surface site-specific interactions of aspartate with
955 calcite during dissolution: Implications for biomineralization. *Am. Mineral.* **82**,
956 878–887 (1997).
957 40. Rodríguez-Navarro, A. B., Marie, P., Nys, Y., Hincke, M. T. & Gautron, J.
958 Amorphous calcium carbonate controls avian eggshell mineralization: A new
959 paradigm for understanding rapid eggshell calcification. *J. Struct. Biol.* **190**,
960 291–303 (2015).
961 41. Beniash, E., Aizenberg, J., Addadi, L. & Weiner, S. Amorphous calcium
962 carbonate transforms into calcite during sea urchin larval spicule growth. *Proc.*
963 *R. Soc. B Biol. Sci.* **264**, 461–465 (1997).
964 42. Ihli, J. *et al.* Dehydration and crystallization of amorphous calcium carbonate
965 in solution and in air. *Nat. Commun.* **5**, 1–10 (2014).
966 43. Mehta, N., Gaëtan, J., Giura, P., Azaïs, T. & Benzerara, K. Detection of
967 biogenic amorphous calcium carbonate (ACC) formed by bacteria using FTIR
968 spectroscopy. *Spectrochim. Acta - Part A Mol. Biomol. Spectrosc.* **278**, 121262
969 (2022).
970 44. Ryparová, P., Prošek, Z., Schreiberová, H., Bílý, P. & Tesárek, P. The role of
971 bacterially induced calcite precipitation in self-healing of cement paste. *J.*
972 *Build. Eng.* **39**, (2021).
973 45. Schmidt, M. P., Ilott, A. J., Phillips, B. L. & Reeder, R. J. Structural changes

upon dehydration of amorphous calcium carbonate. *Cryst. Growth Des.* **14**, 938–951 (2014).

46. Rodríguez-Navarro, A. B. *et al.* Role of the Organic Matter in the Structural Organization of Giant Barnacle Austromegabalanus Psittacus Shell from the Micro- To Nanoscale. *Cryst. Growth Des.* **21**, 357–365 (2021).

47. Valverde, J. M., Perejon, A., Medina, S. & Perez-Maqueda, L. A. Thermal decomposition of dolomite under CO2: Insights from TGA and in situ XRD analysis. *Phys. Chem. Chem. Phys.* **17**, 30162–30176 (2015).

48. Cölfen, H. & Antonietti, M. Mesocrystals: Inorganic superstructures made by highly parallel crystallization and controlled alignment. *Angew. Chemie - Int. Ed.* **44**, 5576–5591 (2005).

49. Bergström, L., Sturm née Rosseeva, E. V., Salazar-Alvarez, G. & Cölfen, H. Mesocrystals in biominerals and colloidal arrays. *Acc. Chem. Res.* **48**, 1391–1402 (2015).

50. Towe, K. M. & Thompson, G. R. The structure of some bivalve shell carbonates prepared by ion-beam thinning - A Comparison Study. *Calcif. Tissue Res.* **10**, 38–48 (1972).

51. Rodriguez-Navarro, C., Ruiz-Agudo, E., Luque, A., Rodriguez-Navarro, A. B. & Ortega-Huertas, M. Thermal decomposition of calcite: Mechanisms of formation and textural evolution of CaO nanocrystals. *Am. Mineral.* **94**, 578–593 (2009).

52. Li, H. *et al.* Calcite prisms from mollusk shells (Atrina rigida): Swiss-cheese-like organic-inorganic single-crystal composites. *Adv. Funct. Mater.* **21**, 2028–2034 (2011).

53. Li, H., Xin, H. L., Muller, D. A. & Estroff, L. A. Visualizing the 3D Internal Structure of Agarose Hydrogels. *Science (80-.).* **326**, 1244–1247 (2009).

1000 54. Nebel, H., Neumann, M., Mayer, C. & Epple, M. On the structure of amorphous
1001 calcium carbonate - A detailed study by solid-state NMR spectroscopy. *Inorg.*
1002 *Chem.* **47**, 7874–7879 (2008).
1003 55. Chaloupecká, E., Tyrpekl, V., Bártová, K., Nishiyama, Y. & Dračínský, M. NMR
1004 crystallography of amino acids. *Solid State Nucl. Magn. Reson.* **130**, (2024).
1005 56. Pisklak, D. M. I., Szeleszczuk, Ł. & Wawer, I. 1H and 13C magic-angle
1006 spinning nuclear magnetic resonance studies of the chicken eggshell. *J. Agric.*
1007 *Food Chem.* **60**, 12254–12259 (2012).
1008 57. Kababya, S., Ben Shir, I. & Schmidt, A. From molecular level to macroscopic
1009 properties: A solid-state NMR biomineralization and biomimetic exploration.
1010 *Curr. Opin. Colloid Interface Sci.* **62**, 101630 (2022).
1011 58. Rietveld, H. M. Line profiles of neutron powder-diffraction peaks for structure
1012 refinement. *Acta Crystallogr.* **22**, 151–152 (1967).
1013 59. Pokroy, B. *et al.* Anisotropic lattice distortions in biogenic calcite induced by
1014 intra-crystalline organic molecules. *J. Struct. Biol.* **155**, 96–103 (2006).
1015 60. Pokroy, B., Fitch, A. N. & Zolotoyabko, E. The microstructure of biogenic
1016 calcite: A view by high-resolution synchrotron powder diffraction. *Adv. Mater.*
1017 **18**, 2363–2368 (2006).
1018 61. Aizenberg, J., Hanson, J., Koetzle, T. F., Weiner, S. & Addadi, L. Control of
1019 macromolecule distribution within synthetic and biogenic single calcite
1020 crystals. *J. Am. Chem. Soc.* **119**, 881–886 (1997).
1021 62. Lang, A. *et al.* Acidic Monosaccharides become Incorporated into Calcite Single
1022 Crystals**. *Chem. - A Eur. J.* **26**, 16860–16868 (2020).
1023 63. Albéric, M. *et al.* Interplay between Calcite, Amorphous Calcium Carbonate,
1024 and Intracrystalline Organics in Sea Urchin Skeletal Elements. *Cryst. Growth*
1025 *Des.* **18**, 2189–2201 (2018).

1026 64. Stevenson, H. P. *et al.* Use of transmission electron microscopy to identify
1027 nanocrystals of challenging protein targets. *Proc. Natl. Acad. Sci. U. S. A.* **111**,
1028 8470–8475 (2014).
1029 65. Schultze-Lam, S. & Beveridge, T. J. Nucleation of Celestite and Strontianite on
1030 a Cyanobacterial S-Layer. *Appl. Environ. Microbiol.* **60**, (1994).
1031 66. Rodriguez-Navarro, C. *et al.* The multiple roles of carbonic anhydrase in
1032 calcium carbonate mineralization. *CrystEngComm* **21**, 7407–7423 (2019).
1033 67. Murdock, J. N. & Wetzel, D. L. FT-IR microspectroscopy enhances biological
1034 and ecological analysis of algae. *Appl. Spectrosc. Rev.* **44**, 335–361 (2009).
1035 68. Ji, Y. *et al.* DFT-Calculated IR Spectrum Amide I, II, and III Band Contributions
1036 of N-Methylacetamide Fine Components. *ACS Omega* vol. 5 8572–8578 at
1037 https://doi.org/10.1021/acsomega.9b04421 (2020).
1038 69. Kim, Y. Y. *et al.* An artificial biomineral formed by incorporation of copolymer
1039 micelles in calcite crystals. *Nat. Mater.* **10**, 890–896 (2011).
1040 70. Seto, J. *et al.* Structure-property relationships of a biological mesocrystal in
1041 the adult sea urchin spine. *Proc. Natl. Acad. Sci. U. S. A.* **109**, 3699–3704
1042 (2012).
1043 71. Cosmidis, J. & Benzerara, K. Comptes Rendus Géoscience Why do microbes
1044 make minerals ? *Comptes Rendus - Géoscience Sci. la Planète* **354**, 0–39
1045 (2022).
1046 72. Mugwar, A. J. & Harbottle, M. J. Toxicity effects on metal sequestration by
1047 microbially-induced carbonate precipitation. *J. Hazard. Mater.* **314**, 237–248
1048 (2016).
1049 73. Albéric, M. *et al.* The Crystallization of Amorphous Calcium Carbonate is
1050 Kinetically Governed by Ion Impurities and Water. *Adv. Sci.* **5**, (2018).
1051 74. Dupraz, C. *et al.* Processes of carbonate precipitation in modern microbial

1052 mats. *Earth-Science Rev.* **96**, 141–162 (2009).
1053 75. Couradeau, E. *et al.* An Early-Branching Microbialite Cyanobacterium Forms
1054 Intracellular Carbonates. 459–463 (2012).
1055 76. Supuran, C. T. & Capasso, C. An overview of the bacterial carbonic
1056 anhydrases. *Metabolites* **7**, (2017).
1057 77. Kocot, K. M., Aguilera, F., McDougall, C., Jackson, D. J. & Degnan, B. M. Sea
1058 shell diversity and rapidly evolving secretomes: Insights into the evolution of
1059 biomineralization. *Front. Zool.* **13**, 1–10 (2016).
1060 78. Soucy, S. M., Huang, J. & Gogarten, J. P. Horizontal gene transfer: Building
1061 the web of life. *Nat. Rev. Genet.* **16**, 472–482 (2015).
1062 79. Sieber, K. B., Bromley, R. E. & Dunning Hotopp, J. C. Lateral gene transfer
1063 between prokaryotes and eukaryotes. *Exp. Cell Res.* **358**, 421–426 (2017).
1064 80. Kahil, K. *et al.* Cellular pathways of calcium transport and concentration
1065 toward mineral formation in sea urchin larvae. *Proc. Natl. Acad. Sci. U. S. A.*
1066 **117**, 30957–30965 (2020).
1067 81. Taylor, A. R., Brownlee, C. & Wheeler, G. Coccolithophore Cell Biology:
1068 Chalking Up Progress. *Ann. Rev. Mar. Sci.* **9**, 283–310 (2017).
1069 82. Gould, S. B., Garg, S. G. & Martin, W. F. Bacterial Vesicle Secretion and the
1070 Evolutionary Origin of the Eukaryotic Endomembrane System. *Trends*
1071 *Microbiol.* **24**, 525–534 (2016).
1072 83. Margulis, L. & Bermudes, D. Symbiosis as a mechanism of evolution: status of
1073 cell symbiosis theory. *Symbiosis* **1**, 101–124 (1985).
1074 84. Gilbert, P. U. P. A. *et al.* Biomineralization by particle attachment in early
1075 animals. *Proc. Natl. Acad. Sci. U. S. A.* **116**, 17659–17665 (2019).
1076 85. Clark, M. S. Molecular mechanisms of biomineralization in marine
1077 invertebrates. *J. Exp. Biol.* **223**, (2020).

1078 86. Barabesi, C. *et al.* Bacillus subtilis gene cluster involved in calcium carbonate
1079 biomineralization. *J. Bacteriol.* **189**, 228–235 (2007).
1080 87. Markgraf, S. A. & Reeder, R. J. High-temperature structure refinements of
1081 calcite and magnesite. *Am. Mineral.* **70**, 590–600 (1985).
1082